Chapter 3 ***Structural, Optical and Magnetization reversal in $CeCr_{1-x}Fe_xO_3$ (x = 0 and 0.05) nanoparticles***

3.1 Introduction

In this chapter, we have investigated the structural, optical, and magnetic properties of $CeCr_{1-x}Fe_xO_3$ (x = 0 and 0.05), synthesized via the solution combustion method. The structural analysis is discussed in section 3.2, which indicates the distortion in the orthorhombic structure, as confirmed through Raman mode analysis detailed in section 3.3. The optical band gap analysis has been conducted through UV-Visible spectra, which suggests a decrease in the band gap after the substitution of Fe. The analysis of absorbance spectra through the Tauc plot is discussed in section 3.4. The unusual magnetic transition T_N, T_{comp}, and T_{SR}, along with the presence of magnetization reversal in $CeCr_{1-x}Fe_xO_3$ (x = 0 and 0.05) nanoparticle, have been observed from temperature-dependent magnetization measurement, which is discussed in section 3.5. The negative magnetization is further analyzed through fitting using the empirical formula formulated by A. H. Cooke, which is discussed in section 3.5.2. We have also discussed the field-assisted stable bipolar switching behavior of magnetization in section 3.5.3, which makes these materials a potential candidate for spin resolving and magnetic switching devices. The important findings of this chapter are summarized in section 3.6.

3.2 Structure and microstructure

3.2.1 Structural analysis

Room temperature XRD patterns of $CeCr_{1-x}Fe_xO_3$ (x = 0 and 0.05) depicted in figure 3.1 show well distinguished and sharp diffraction peaks indicating the crystalline nature of particles.

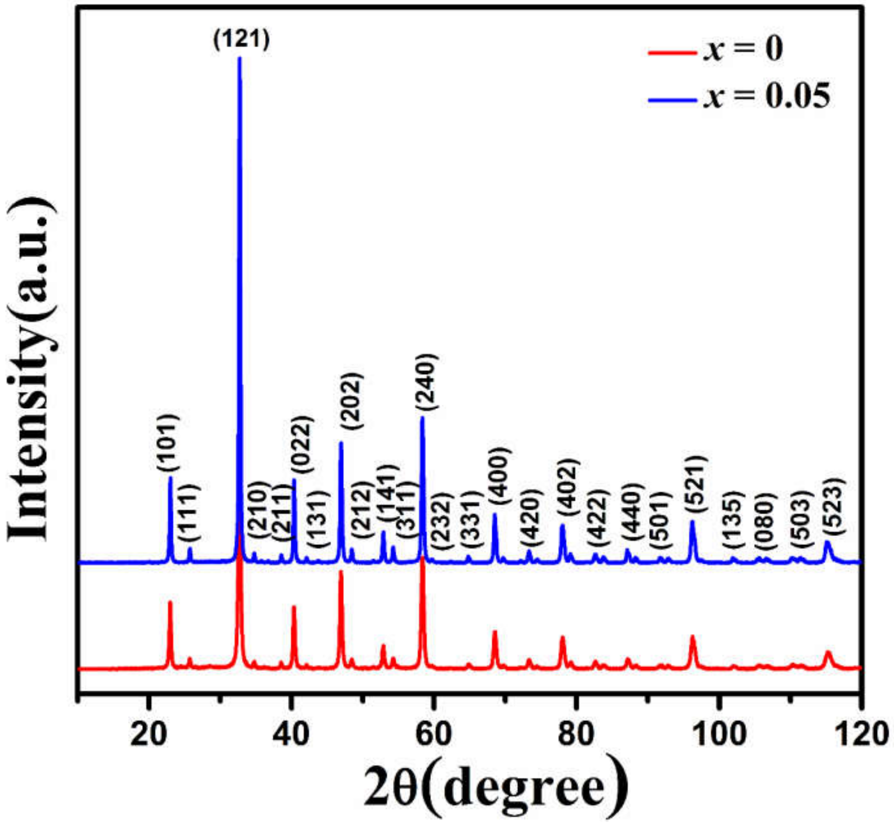

Figure 3.1 Powder X-Ray diffraction patterns of $CeCr_{1-x}Fe_xO_3$ (x = 0 and 0.05) compound recorded at room temperature.

The observed diffraction peaks are indexed based on the JCPDS card # 898770 for the space group, *Pnma*. It is to be noted that no other peaks corresponding to any impurity phase are observed after the substitution of Fe^{3+} in $CeCrO_3$ lattice, thus, confirming the pure orthorhombic phase. Further, XRD patterns are fitted with the Rietveld refinement of Full-Prof program using the *Pnma* space group (figure 3.2a and 3.2b). The experimental, calculated, and their difference patterns are denoted as a solid line, dot, and continuous bottom line, respectively. The position of Bragg reflections represented by the tick marks above the difference pattern indicates the reflection planes of the orthorhombic phase. Structural parameters determined from the Rietveld refinement using pseudo-voigt as peak profile function are listed in Table 3.1 and the refined structure are shown in Figure 3.3.

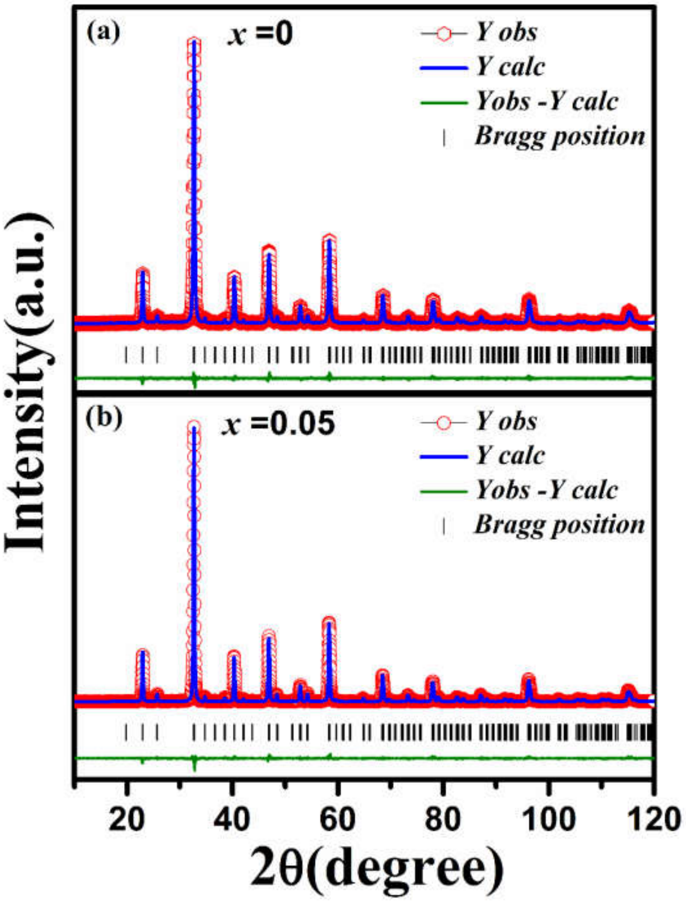

Figure 3.2 Rietveld refinement of XRD patterns along with the difference pattern between observed and calculated one of $x = 0$(a) and 0.05(b).

Table 3.1 Structural parameter of $CeCr_{1-x}Fe_xO_3$(x=0 and 0.05) nanoparticles.

Compound	$CeCrO_3$	$CeCr_{0.95}Fe_{0.05}O_3$
a(Å)	5.4743(3)	5.47917(16)
b(Å)	7.7340(3)	7.73658(18)
c(Å)	5.4802(3)	5.48252(17)
V(Å)^3	232.02	232.40
Ce(4c)		
x	0.02738(10)	0.02924(10)
y	0.25	0.25
z	-0.0066(2)	-0.00656(17)
B_{iso}	0.134	0.134
Cr/Fe(4b)		
x	0.00	0.00
y	0.00	0.00
z	0.50	0.50
B_{iso}(Cr)	0.233	0.233
B_{iso}(Fe)	-	0.232
O1(4c)		
x	0.4878(14)	0.4872(13)
y	0.25	0.25
z	0.075(2)	0.074(2)
B_{iso}	0.450	0.450
O2(8d)		
x	0.281(2)	0.2819(18)
y	0.0333(14)	0.0354(10)
z	0.720(2)	0.7169(17)
B_{iso}	0.450	0.450
Reliability factor of goodness of fit		
χ^2	1.19	1.29
R_P	7.87	7.40
R_{wp}	11.3	11.3
a_P	3.072	3.074

The cell parameters are found to increase with the incorporation of Fe in $CeCrO_3$, leading to an increase in cell volume from 232.02 Å^3 to 232.40 Å^3. The expected distortion in $CeCrO_3$ structure is determined using the Goldschmidt tolerance factor, $t = (< Ce - O >)/\{\sqrt{2}(< Cr - O >)\}$. The 't' is estimated to be 0.922 and 0.919 for x = 0 and 0.05, respectively which is within the reported limit of (RE)CrO_3 perovskite structure with orthorhombic symmetry (0.93 to 0.85) [106]. The decrease in 't' factor is very small to ascribe it as distortion of orthorhombic structure. Further, the difference in bond angle Cr(Fe)-O(1)-Cr(Fe) and Cr(Fe)-O2-Cr(Fe) demonstrates change in the angular distortions <ω>. The angular distortions < ω > of CrO_6 octahedra are estimated from the relation <ω> = 180 - < Cr(Fe)-O-Cr(Fe) > are found to increase from 22.40° to 22.86° when x increase from 0 to 0.05 [Table 3.2]. Similar distortions have been discussed by Nandy et al. in $NdMnO_3$ system after substitution of monovalent cation[107].

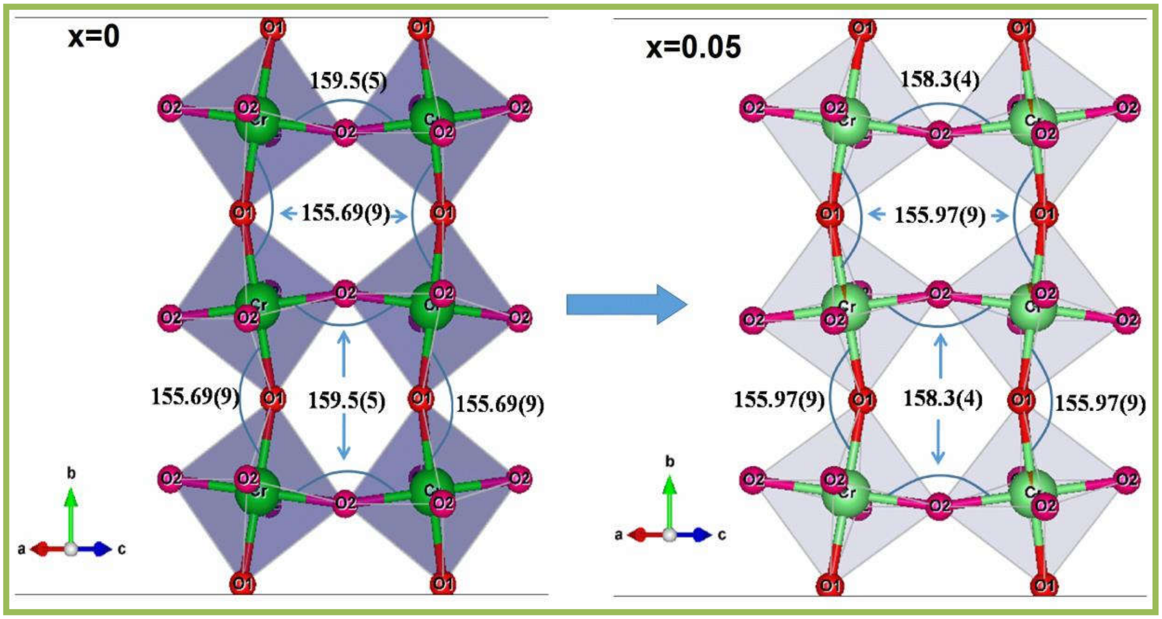

Figure 3.3 Bond angle between two adjacent octahedral Cr-O1-Cr and Cr-O2-Cr of $CeCr_{1-x}Fe_xO_3$ ($x = 0$ and 0.05) using VISTA software.

Since oxygen positional parameters are almost identical within the error bar, the observed weak distortion of the Cr(Fe)-O-Cr(Fe) can be due to the sheer consequence of lattice expansion. The distortion in perovskite structure is contributed either due to the co-operative tilting of octahedral or due to the Jahn-Teller active element present in the perovskite.

Table 3.2 Bond angles and bond lengths of $CeCr_{1-x}Fe_xO_3$ (x = 0.0 and 0.05) compounds obtained from the Rietveld structure refinements of XRD patterns.

Compound	**$CeCrO_3$**	**$CeCr_{0.95}Fe_{0.05}O_3$**
Cr(Fe)-O1-Cr(Fe)	155.69(9)	155.97(9)
Cr(Fe)-O2-Cr(Fe)	159.5(5)	158.3(4)
$<\omega_1>$	24.31	24.03
$<\omega_2>$	20.5	21.7
$<\omega>$	22.4	22.86
Cr(Fe)-O1 (×2)	1.978(2)	1.977(2)
Cr(Fe)-O2 (×2)	1.971(11)	1.969(10)
Cr(Fe)-O2’ (×2)	1.964(11)	1.977(9)
<Cr-O>	1.971	1.974
$\Delta_{(Cr-O)}$	0.066×10^{-4}	0.11×10^{-4}
Ce-O1	2.560(8)	2.548(7)
Ce-O1	2.375(11)	2.383(11)
Ce-O2 (×2)	2.642(11)	2.640(9)
Ce-O2 (×2)	2.449(11)	2.434(9)
Ce-O2 (×2)	2.728(11)	2.729(8)
<Ce-O>	2.57125	2.56713
$\Delta_{(Ce-O)}$	24.13×10^{-4}	25.18×10^{-4}
‘t’	0.922	0.919
Φ[010]	6.99	7.45
Θ[101]	12.15	12.02

In the $CeCrO_3$, since Cr^{3+} is a Jahn-Teller (JT) inactive cation, therefore, causing almost no dispersion in the Cr-O bonds and the distortion is only contributed by the co-operative tilting of octahedra. Further, we have calculated the octahedra tilt angles θ and ϕ using the equation given below as formulated previously [108,109]

$$\theta = \arctan\left[4 \times \frac{\sqrt{w_{O(1)}^2 + u_{O(1)}^2}}{b}\right] \qquad [3.1]$$

$$\phi = \arctan\left[4 \times \frac{\sqrt{w_{o(2)}^2 + u_{o(2)}^2}}{\sqrt{c^2 + a^2}}\right] \qquad [3.2]$$

Where 'w' and 'u' are the atomic displacement (in Å) of O1 and O2, respectively, and a, b, and c are the lattice parameters [108]. Tilt angles θ and ϕ describe the octahedral rotations around the [101] and [010] axes, respectively. Both θ and ϕ for x = 0 and 0.05 are listed in Table 2. It is well known that by reducing the ionic radii of R^{3+}ion, tilting (θ and ϕ) increases [108]. From $LaCrO_3$ to $NdCrO_3$ with decreasing ionic radii from 1.160Å (La^{3+}) to 1.109Å (Nd^{3+}), tilt angles θ and ϕ increases from 10.92° to 13.86°and 5.25° to 7.55°, respectively. As the ionic radius of Ce^{3+} (1.143Å) is in between the ionic radius of Nd^{3+}(1.109Å) and La^{3+}(1.160Å), we observe the tilt angles θ and ϕ of pristine $CeCrO_3$ lying in between the tilt angles θ and ϕ of $LaCrO_3$ and $NdCrO_3$. However, after the substitution of Fe^{3+}, the value of tilt angle θ slightly decreases from 12.16° to 12.02° whereas the tilt angle ϕ increases from 6.99° to 7.45°. Such change in θ and ϕ supports the weak distortion. From Bragg peak broadening, crystallite size and lattice strain are estimated using Williamson–Hall method. According to this method, x-ray diffraction peak broadening $\beta_{hkl} = \beta_{size} + \beta_{strain}$. The actual peak broadening (β) is obtained by correcting the experimental peak broadening (β_{exp}) and the instrumental broadening (βins) as $\beta_{hkl}^2 = \beta_{exp}^2 - \beta_{ins}^2$. β_{ins} is the broadening due to the instrument, where β_{ins} was obtained from the silicon powder standard using the angular dependence proposed by Caglioti et al. according to equation [110,111]:

$$\beta_{ins} = \sqrt{U tan^2\theta + V tan\theta + W} \quad [3.3]$$

Hence, XRD peak broadening $\beta_{hkl} = \beta_{size} + \beta_{strain}$ equation can be in modified form as[110]:

$$\beta_{hkl} = \frac{0.9\lambda}{D cos\theta} + 4\varepsilon\, tan\theta \quad [3.4]$$

$$\beta_{hkl} cos\theta = \frac{0.9\lambda}{D} + 4\varepsilon\, sin\theta \quad [3.5]$$

where β is full width at half maximum (FWHM) in radians, k is shape parameter (~ 0.9 for arbitrary shape), θ is the Bragg angle, D is the crystallite size, λ is the wavelength of the X-rays and ε is the lattice strain. βcosθ vs. 4sinθ is shown in figure 3.4 for $x = 0$ and 0.05. For pure particle size broadening, while the plot shows a straight line parallel to 4sinθ axis, the non-zero slope indicates the presence of strain in the lattice. From the non-zero slope we estimate that the crystallite size increases from 36.2 to 46.3 nm while strain decreases from 9.89×10^{-4} to 8.64×10^{-4}.

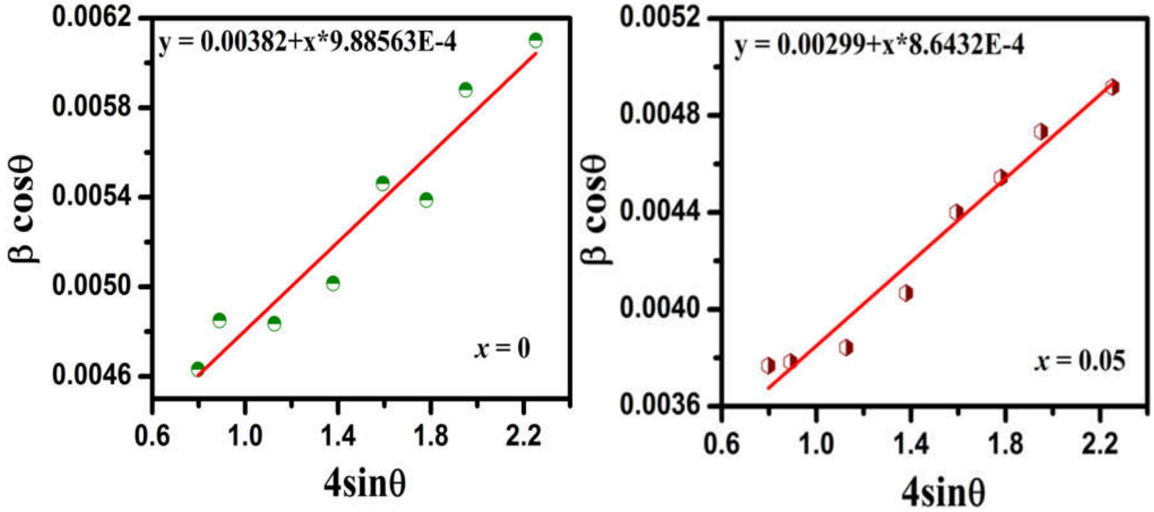

Figure 3.4 Plot between βcosθ and 4sinθ of $CeCr_{1-x}Fe_xO_3$ ($x = 0$ and 0.05).

3.2.2 Microstructural analysis

Further, the size and morphology of $x = 0$ and 0.05 nanoparticles are determined using the TEM micrographs. The particles are found to be agglomerated and semispherical in shape (figure 3.5). The particle size distribution histogram reveals the average particle size of approximately 45 nm for $x = 0$ and approximately 66 nm for $x = 0.05$ (inset of figure 3.5). Comparing the crystallite size and particle size, it is confirmed that both compositions are polycrystalline in nature. Although size of the particle is controlled by nucleation and growth process, nevertheless the lattice parameter of Fe doped sample is higher than the undoped one. The particle size is decided by the nucleation and growth processes; therefore, after doping with Fe, the growth must dominate the nucleation process, which could be the reason behind the increase in particle size.

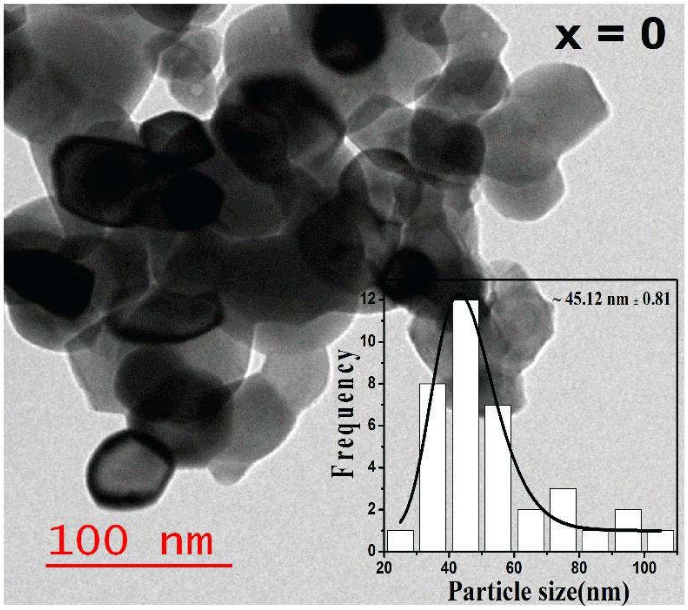

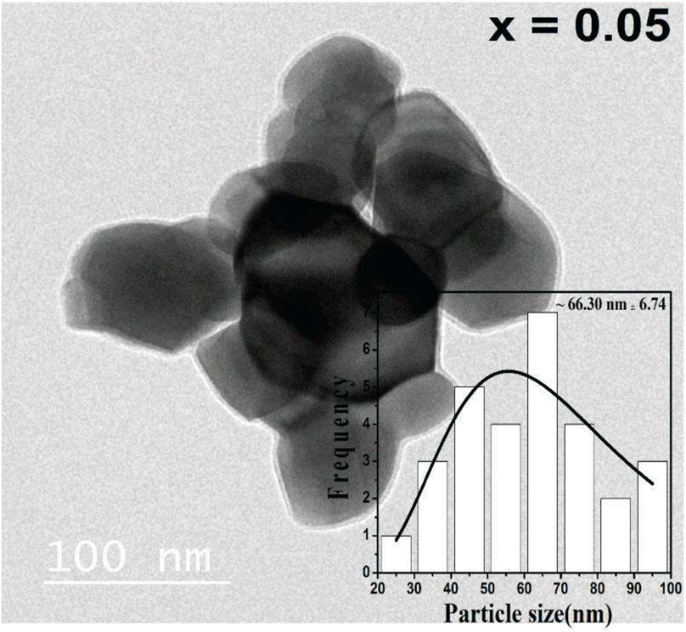

Figure 3.5 Transmission electron micrographs of *x* = 0 and 0.05 along with particle size histogram shown in the inset of the respective micrographs.

3.3 Raman analysis

Further structural characteristics examined through Raman spectroscopy at room temperature are shown in Figure 3.6. According to the group theory, this orthorhombic Pnma structure with four formula units per unit cell gives rise to 24 Raman active modes: ($7A_g + 5B_{1g} + 7B_{2g} + 5B_{3g}$) [108]. Here we observe five Raman modes present within 100–750 cm^{-1} for the orthorhombic *Pnma* $CeCrO_3$ perovskite. The other modes are either too weak in intensity or have energies below the experimental cut-off wave number. The observed peaks at 350.1, 352.3, 408.7, 450.5, and 543 cm^{-1} are corresponding to $A_g(5)$, $B_{1g}(2)$, $B_{2g}(3)$, $A_g(6)$, and $B_{3g}(3)$ modes, respectively. While modes below 200 cm^{-1} are related to vibrations of R atoms, the modes above 200 cm^{-1} correspond to the vibrations of the R atom and oxygen. For instance, $A_g(5)$ are octahedral rotations around the x-axis (Pnma setting); $A_g(6)$ and $B_{2g}(3)$ arise due to the bending of the Cr-O_6 octahedra and the $B_{1g}(2)$ mode is due to R shift. Further, it is noticed that the phonon frequency of the $A_g(6)$ mode changes from 451 cm^{-1} ($x = 0$) to 444 cm^{-1} ($x = 0.05$) in addition to less shifting in other modes as well. $A_g(6)$ mode is associated with the bending of the Cr-O_6 octahedra, which results in the rotation of the Cr-O_6 octahedra in [010] plane. Such type of bending of octahedra is also discussed by *Xiang et al.* in $SmFe_{1-x}Cr_xO_3$ compound [112]. Thus the bending of Cr-O_6 octahedra is a consequence of the lattice expansion.

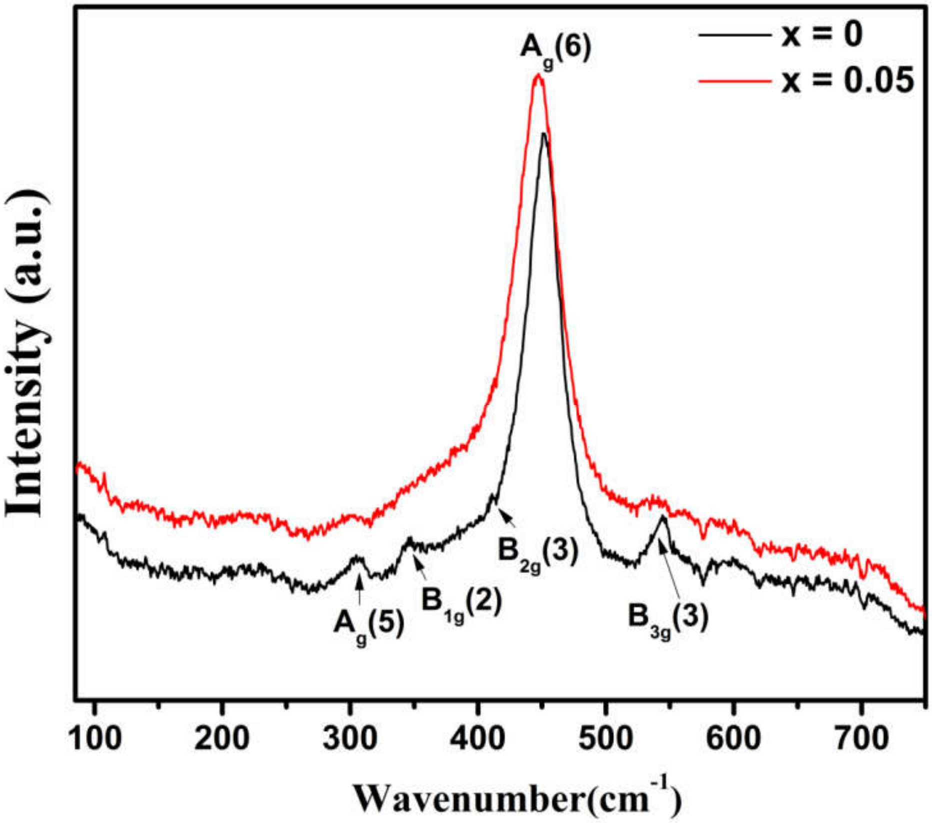

Figure 3.6 Raman spectra recorded at room temperature, using 473 nm diode laser of $CeCr_{1-x}Fe_xO_3$ ($x = 0$ and 0.05).

3.4 UV visible spectroscopy

The absorbance of $CeCr_{1-x}Fe_xO_3$ ($x = 0$ and 0.05) compounds depicted in figure 3.7 show the strong absorption in both ultraviolet and visible wavelength range. In UV range, two peaks are found at 235 and 300 nm, whereas in the visible range, three peaks at 465, 610 and 742 nm are observed. In $RCrO_3$, while the absorption peaks below 400 nm are attributed to 4f-5d and charge transfer transitions [113], the absorption peaks above 400 nm are due to optical transition of Cr^{3+} $3d^3$ electrons in octahedral crystal field of Cr-O_6 [77,114]. For octahedrally coordinated Cr^{3+}, there are three spin-allowed transitions: ${}^4A_{2g}$ to ${}^4T_{1g}$, ${}^4A_{2g}$ to ${}^4T_{2g}$ of term ${}^4F$ and ${}^4A_{2g}$ to ${}^4T_{1g}(p)$ of term ${}^4P$. In addition, there are two spin-forbidden transitions: ${}^4A_{2g}$

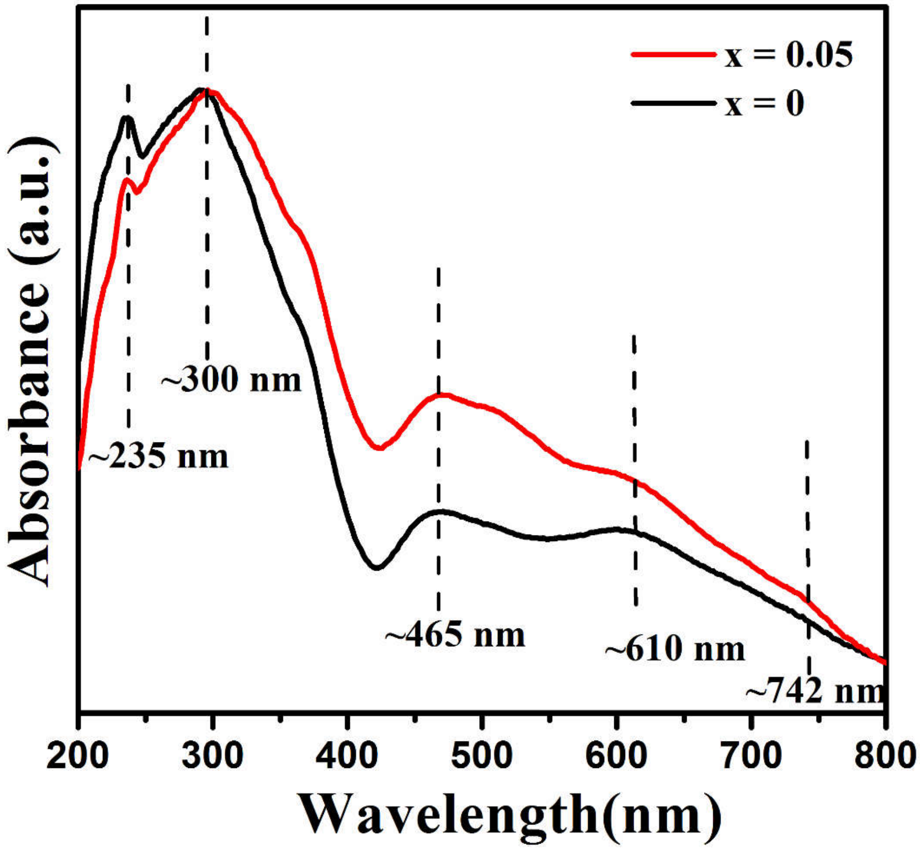

Figure 3.7 UV-Visible absorbance spectra of $CeCr_{1-x}Fe_xO_3$(x =0, 0.05)

to $^2T_{1g}$ and $^4A_{2g}$ to ^2E_g. In our case the two dominant peaks observed at 465 nm and 610 nm results from $^4A_{2g}$ to $^4T_{1g}$ and $^4A_{2g}$ to $^4T_{2g}$ transitions, respectively. A weak peak at 742 nm corresponds to a spin forbidden transition $^4A_{2g}$ to ^2E_g. Further, we have calculated the band gap using the Tauc plot as shown in figure 3.8 (a) and (b) for x = 0 and 0.05, respectively.

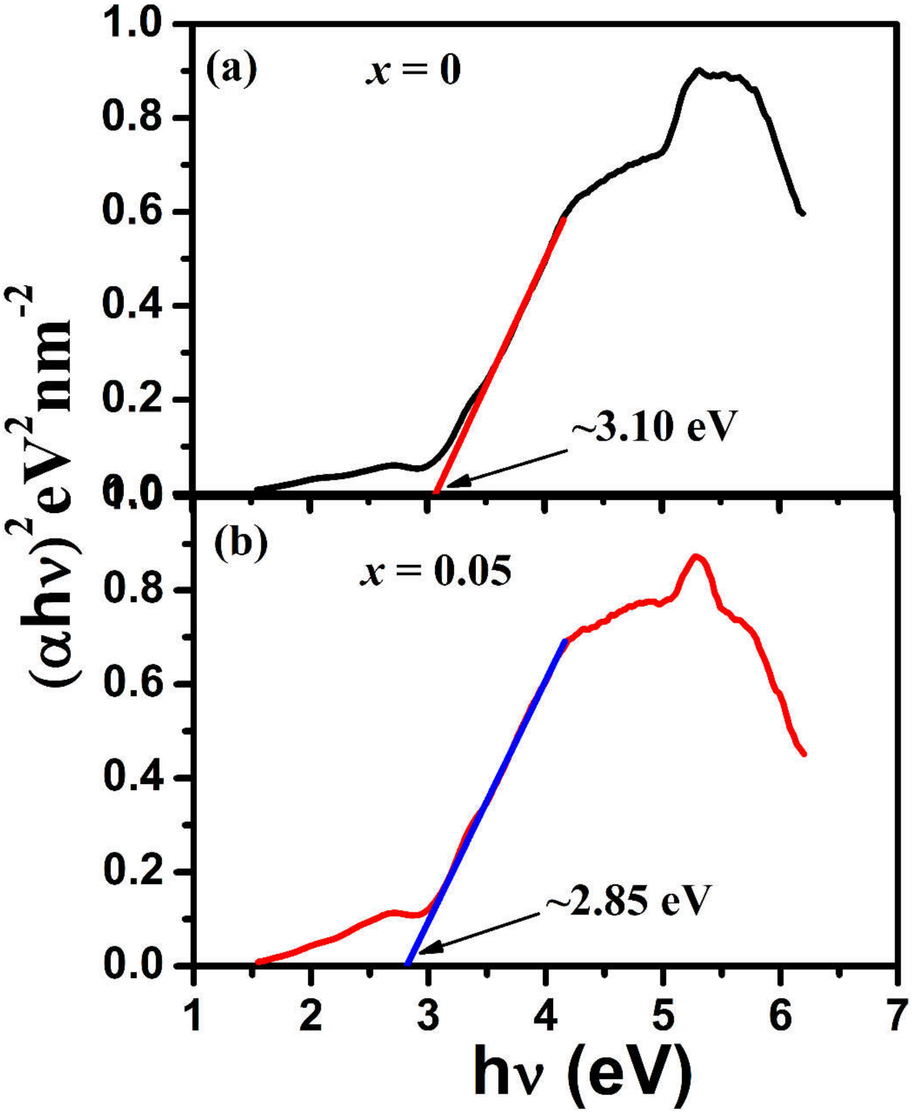

Figure 3.8 (a) and (b)Band gap analysis using Tauc plot from absorbance spectra of x = 0 and x = 0.05, respectively.

The band gap is found to be 3.10 eV for $x = 0$ and 2.85 eV for $x = 0.05$. The decrease in optical band gap evidently suggests that Fe^{3+}cation substituted for Cr^{3+}cation influences the Cr–O overlap integral. Similar observation in $NdCrO_3$ after doping Bi^{3+} has been reported elsewhere [115]. Besides, after substitution of Fe, the increase in particle size and decrease in strain estimated from Williamson-Hall analysis is accompanied with decrease in band gap as observed here[116,117].

3.5 Magnetic properties

3.5.1 Temperature dependent magnetization

The temperature-dependent magnetization of $CeCrO_3$ measured under zero-field cooled (*ZFC*) and field-cooled (*FC*) modes at different applied fields (i.e. 0.1, 1, 2, and 5 kOe) are shown in figure 3.9(a-d). The magnetization curve recorded in *ZFC* and FC mode for pristine $CeCrO_3$ at 0.1 kOe shows paramagnetic to antiferromagnetic transition, T_N due to the ordering of Cr^{3+} moments at around 260 K (Figure 3.9(a)). The observed T_N is consistent with the T_N ~260 K reported for both bulk and nanoparticles of $CeCrO_3$ by Cao et al. and Taheri et al., respectively [85,91]. Below T_N, M_{FC} (Field-cooled magnetization) increases showing a maximum magnetization at a temperature, T_{max} ~ 215 K. With further decreasing the temperature, M_{FC} decreases monotonously and crosses M_{ZFC} (Zero-field cooled magnetization) at 110 K, known as T_{cross}. The decrease in M_{FC} with the reducing temperature is attributed to the canted antiferromagnetic ordering of Cr^{3+}moments which imposes a local field upon the neighboring Ce^{3+} moments. Hence, the Ce^{3+} moments experience a net local field, which is the superposition of the internal field due to the Cr^{3+} moments and the applied external field. The resultant antiferromagnetic coupling between Ce^{3+} and the canted Cr^{3+} moments polarizes the Ce^{3+} moments antiparallel to the

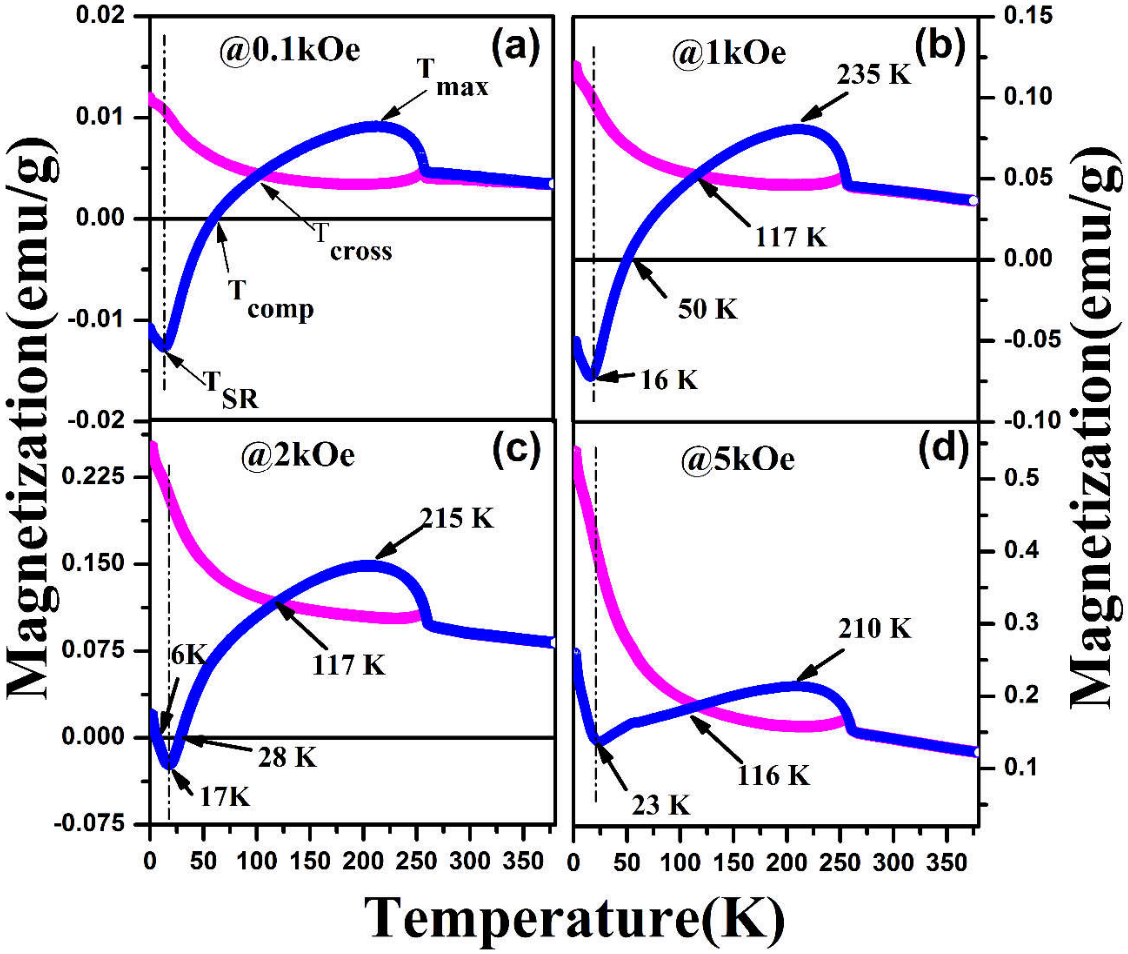

Figure 3.9 Temperature dependent magnetization in ZFC and FC mode under external field of 0.1, 1, 2 and 5 kOe for $x = 0$ shown as in (a), (b), (c), (d) respectively.

ferromagnetic component of the canted Cr^{3+} moment. Therefore, with further decrease in the temperature, the competition between Cr^{3+} and Ce^{3+} moments results in the compensation of the net magnetization which is observed at T_{comp} ~ 61 K. Below T_N, a negative magnetization is observed which approaches a maximum magnitude of 0.0127 emu/g at a temperature known as spin reorientation transition, T_{SR} at 15 K. Similar T_{SR} behavior has been observed in $GdCrO_3$ where the reorientation of Cr^{3+} moments causes the transformation of $\Gamma_4(G_x, A_y, F_z)$ to $\Gamma_2(F_x, C_y, G_z)$ [48]. Further, with increasing external field up to 5 kOe, while T_N ~260 K remains almost same, T_{max} significantly decreases to 210 K. The T_{comp} decreases from 61 to 28 K with the increasing external field from 0.1 to 2 kOe. Interestingly, the decrease in T_{comp} at 2 kOe is accompanied by another T_{comp} observed at 6 K and above this field, no compensation is observed. Besides, we observe an enhancement in T_{SR} to 23 K after increasing the external field up to 5 kOe. As the external field increases, the previously antiparallel Ce^{3+} moments to the Cr^{3+} moments and external field starts aligning in the field direction and, thereby, causing two T_{comp} at the moderate field (i.e 2 kOe) followed by their disappearance at the higher external field. Such behavior could also be attributed to the observed increase in T_{SR}. During *ZFC* measurement, Cr^{+3} and Ce^{+3} ions are uncoupled and experience the same external applied field and therefore, contribute independently to the total magnetization. As a result, a rapid increase in *ZFC* magnetization followed by an antiferromagnetic transition at around 260 K is observed. The increase in magnetization arises from the polarization of Ce^{3+}moment by the Cr^{3+} moment. At the lowest temperature, the slope in magnetization changes which could be due to the ordering of Ce^{3+} moment.

After incorporation of Fe in $CeCrO_3$, along with T_N ~ 253 K due to the antiferromagnetic ordering of Cr^{3+} moments, we observe a new magnetic ordering at around 315 K under *FC* mode of 0.1kOe (figure 3.10(a)). In $CeCr_{1-x}Fe_xO_3$ ($x = 0.05$), different magnetic interactions such as Cr^{3+}-O-Cr^{3+}, Cr^{3+}-O-Fe^{3+}, Fe^{3+}-O-Fe^{3+}, Ce^{3+}-O-Ce^{3+}, Ce^{3+}-O-(Cr^{3+}/ Fe^{3+}) are possible. It is known that Fe^{3+}-O-Fe^{3+} and Ce^{3+}-O-Ce^{3+} orders at ~ 645 K and ~ 1.8 K in $CeFeO_3$, respectively [92]. While Ce^{3+}-O-Ce^{3+} ordering temperature is too low,

Fe^{3+}-O-Fe^{3+}ordering occurs at high temperatures. Therefore, it is reasonable to attribute the

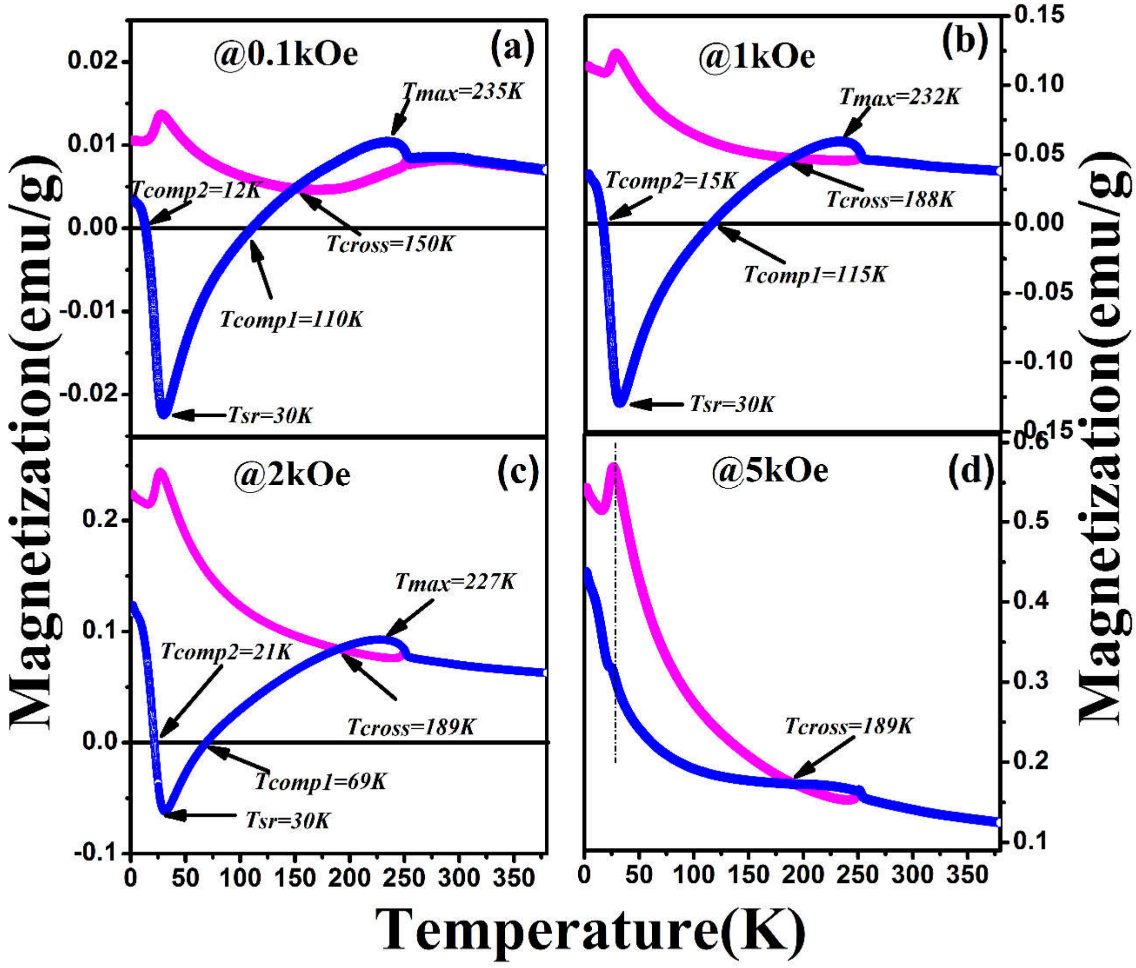

Figure 3.10 Temperature dependent magnetization in ZFC and FC mode under 0.1, 1, 2 and 5 kOe external field for $x = 0.05$ in (a)-(d). (Blue solid line represents FC magnetization and magenta solid line represents ZFC magnetization)

magnetic transition observed at ~ 315 K to the Cr^{3+}-O-Fe^{3+} AFM interaction. Such type of magnetic transition has been discussed in $DyFe_{0.5}Cr_{0.5}O_3$ by Yin et. al [118]. The decrease in antiferromagnetic ordering of Cr^{3+}momentsafter Fe^{3+} substitution from 260 K to 253 K can be attributed to the decrease in a superexchange angle Cr-O2-Cr from 159.5° to 158.3° (Table 3.2) due to the cooperative octahedral rotation.

Below T_N, no significant change in T_{max} (~235 K) is observed after the Fe incorporation. Further, it is observed that with decreasing temperature below T_{max}, both T_{comp1} ~ 110 K and T_{SR} ~ 30 K are almost doubled in comparison to T_{comp}~ 61 K and T_{SR} ~ 15 K in the pristine sample. Besides the doubling of T_{comp1} and T_{SR}, we notice that the magnitude of M_{FC}(~ 0.0225emu/g)at T_{SR} in $x = 0.05$ is also approximately doubled to the M_{FC}(0.012emu/g) at T_{SR} in the pristine sample. Thus, one could argue that below T_{max}, Fe^{3+} as well as Ce^{3+}ions polarizes in the direction opposite to that of ferromagnetic component of canted Cr^{3+} moment and parallel to its internal field direction. Due to the polarization of Fe^{3+} with Ce^{3+} moments, the M_{FC} decreases rapidly below T_{max} which consequently increases the T_{comp1} and T_{SR}.Below T_{SR}, ordering of Ce^{3+} as well as Fe^{3+} moments increases and starts to polarize along the external field direction. Therefore, magnetization increases and becomes positive showing another compensation temperature, T_{comp2}at 13 K which found to be absent in $x = 0$ when the applied field is 0.1 kOe. In order to facilitate the understanding of magnetic transitions in $x = 0.05$, we have presented a pictorial representation of ordering of Cr^{3+}, Ce^{3+} and Fe^{3+}ions with respect to the decrease in temperature from the paramagnetic range as shown In Figure3.11. When the magnetic field is increased to 1 kOe, more Cr^{3+} moment align in the external field direction and impose a large internal field on Ce^{+3} and Fe^{3+} moments. As a result, the net magnetization decreases rapidly and increases the T_{comp1} to 115 K. However, the polarization of Fe^{3+} in field direction does not affect the T_{SR} which is observed at 30 K. Below T_{SR}, the magnetization increases rapidly due to the polarization of Fe^{3+} as well as ordered Ce^{3+} in field direction which causes the increase in T_{comp2} to ~ 15 K. Further increase in field to 2 kOe, whileT_{comp1} decreases to 69 K, T_{comp2} increases to 21 K. The decrease in T_{comp1} and increase inT_{comp2} indicates that the external field has started dominating over the internal field and therefore, causes some of the moments of either Ce^{3+} or Fe^{3+} to align along the applied field direction. At 5 kOe, however, the external field completely dominates over the internal field which results in the absence of negative magnetization and T_{comp}.

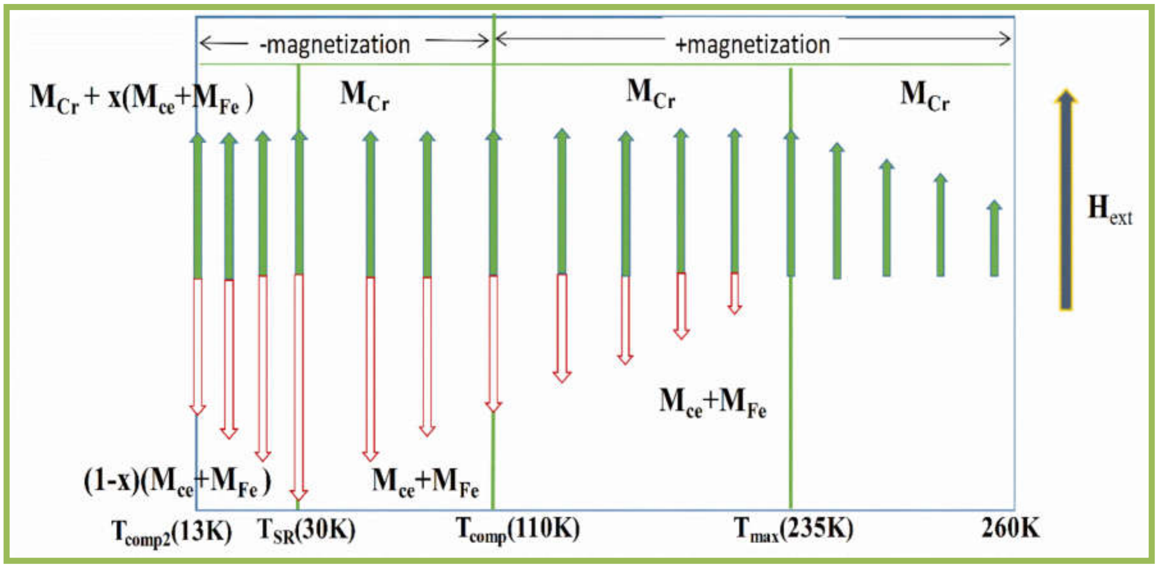

Figure 3.11 Schematic representation of arrangement of Cr^{3+}, Ce^{3+} and Fe^{3+} moments under 0.1 kOe FC mode of $x = 0.05$.

3.5.2 Negative magnetization

In order to understand the sign reversal of magnetization, the *FC* magnetization curve fitted between $T_{SR}<T<T_{\max}$ using the following equation [48]:

$$M = M_{Cr} + \frac{C(H+H_I)}{(T-\theta_C)} \qquad [3.4]$$

Where M is the total magnetization, M_{Cr} is the magnetization due to the week ferromagnetic component of canted Cr^{3+}moment, H_I is the internal magnetic field due to Cr^{3+}moment, C is the Curie constant, and θ_c is Weiss temperature. A typical fitting of FC magnetization under

0.1,1 and 2kOe are shown in figure 3.12 and 3.13, respectively, and the fitted parameters under an applied field of 0.1,1 and 2kOe are tabulated in Table 3.3. The negative sign of H_I indicates that the internal magnetic field due to Cr^{3+}ion is in opposite direction to the applied magnetic field. From Table 3.3, it is also confirmed that the internal magnetic field depends upon the magnitude of applied magnetic field. Both M_{Cr} and negative H_I are found to increase with the increase in the applied field in both $x = 0$ and 0.05.

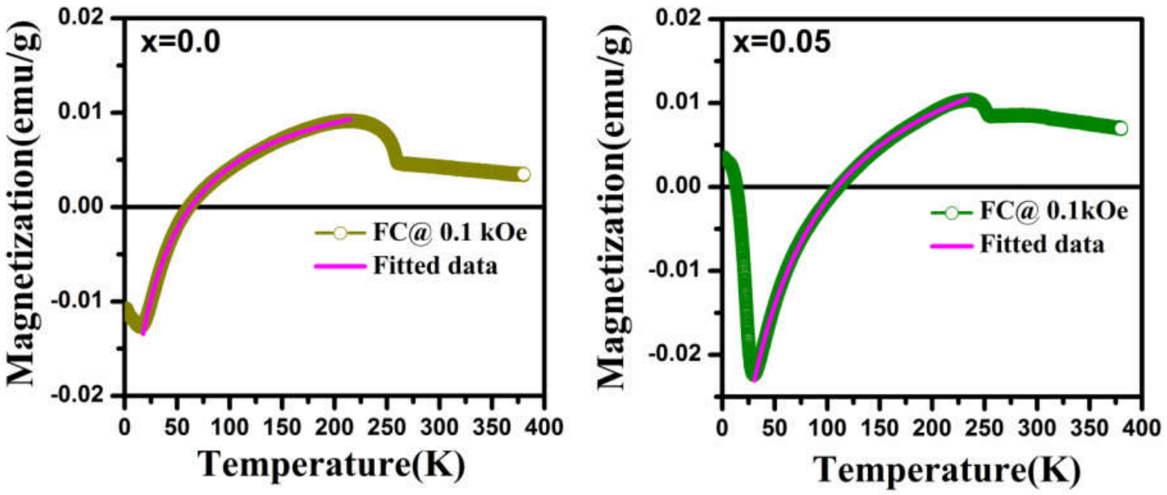

Figure 3.12 FC magnetization curve Fitted between T_{max} to T_{SR} using equation (3.4) of $CeCr_{1-x}Fe_xO_3$ ($x = 0.0$ and 0.05).

This respective changes with the field can be attributed to the increase in AFM ordering with the increase in the applied field that gives rise to an increase in H_I and M_{Cr}. θ_c is found to vary from -33 to -42 K when x=0 and from -52 to -82 K for x= 0.05. The negative value of θ_c endorses the AFM interaction between the canted Cr^{3+}moment and Ce^{3+}moment in $x = 0$ and between the canted Cr^{3+} and Ce^{3+}+Fe^{3+} moment in $x = 0.05$ which increases with the increase in field.

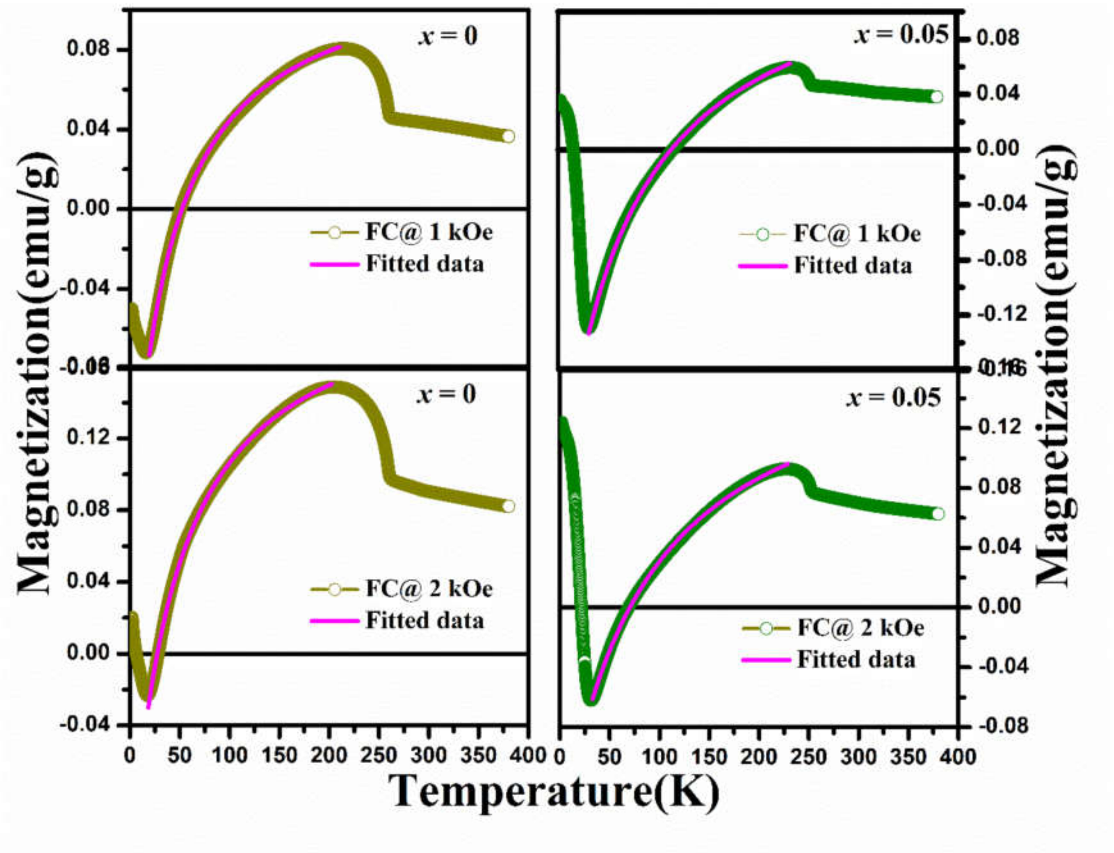

Figure 3.13 FC magnetization curve @ 1 and 2 kOe Fitted between T_{max} to T_{SR} using equation (3.4) of $CeCr_{1-x}Fe_xO_3$ ($x = 0.0$ and 0.05).

Table 3.3 Fitting parameters for magnetization curve under 0.1, 1 and 2kOe FC magnetization curve of $CeCr_{1-x}Fe_xO_3$($x = 0.0$ and 0.05).

External field	$x = 0$	$x = 0.05$
M_{Cr}(emu/g)		
100	0.01518(1)	0.02428(2)
1000	0.12795(11)	0.15655(20)
2000	0.21235(18)	0.18816(31)
H_I(Oe)		
100	-177.21(15)	-211.2(2)
1000	-1623.4(15)	-1954.6(23)
2000	-2425.4(12)	-3128.2(46)

θ_C		
100	-33.64(9)	-52.37(14)
1000	-38.11(12)	-66.53(19)
2000	-44.69(16)	-81.84(36)

3.5.3 Field assisted memory switching application

Owing to the existence of characteristic features like magnetic reversal, $CeCr_{1-x}Fe_xO_3$ (x = 0 and 0.05) has been explored for distinct magnetic switching effect. The temperature dependent magnetization in FC mode taken under -0.1 kOe shows a mirror-like image with the FC measurement under +0.1 kOe as depicted in figure 3.14.

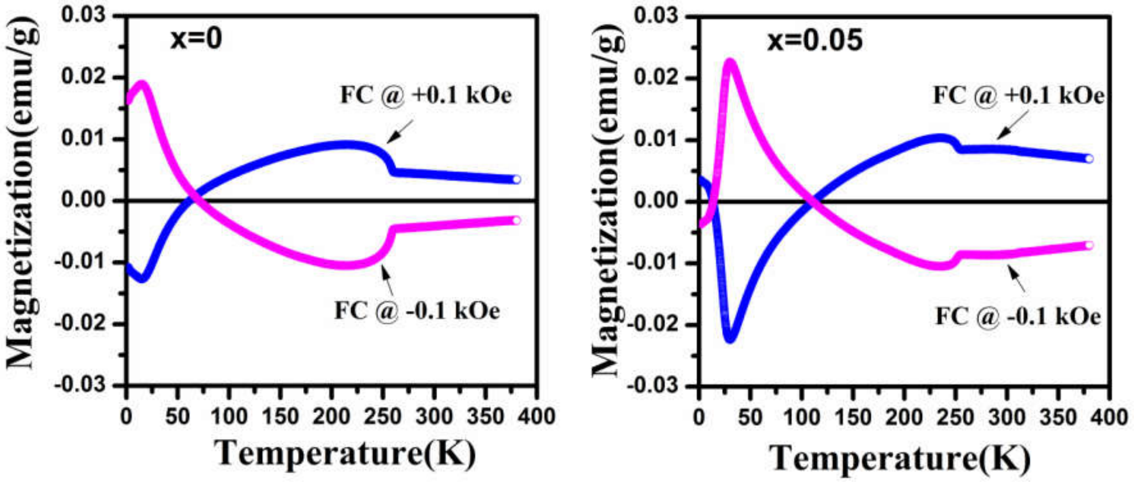

Figure 3.14 Mirror like behaviour observed in FC magnetization curve measured under ±0.1 kOe of $CeCr_{1-x}Fe_xO_3$ (x = 0.0 and 0.05).

One may note that the net magnetic moment is in the direction of the external magnetic field above T_{comp1} and opposite to external magnetic field below T_{comp1}. Prior to the magnetic switching effect, x = 0 sample is field cooled under the applied field of 1 kOe from 380 K to

20 K and then, the switching of magnetization is measured between 1 kOe and 2.3kOe at 20 K as shown in figure 3.15.

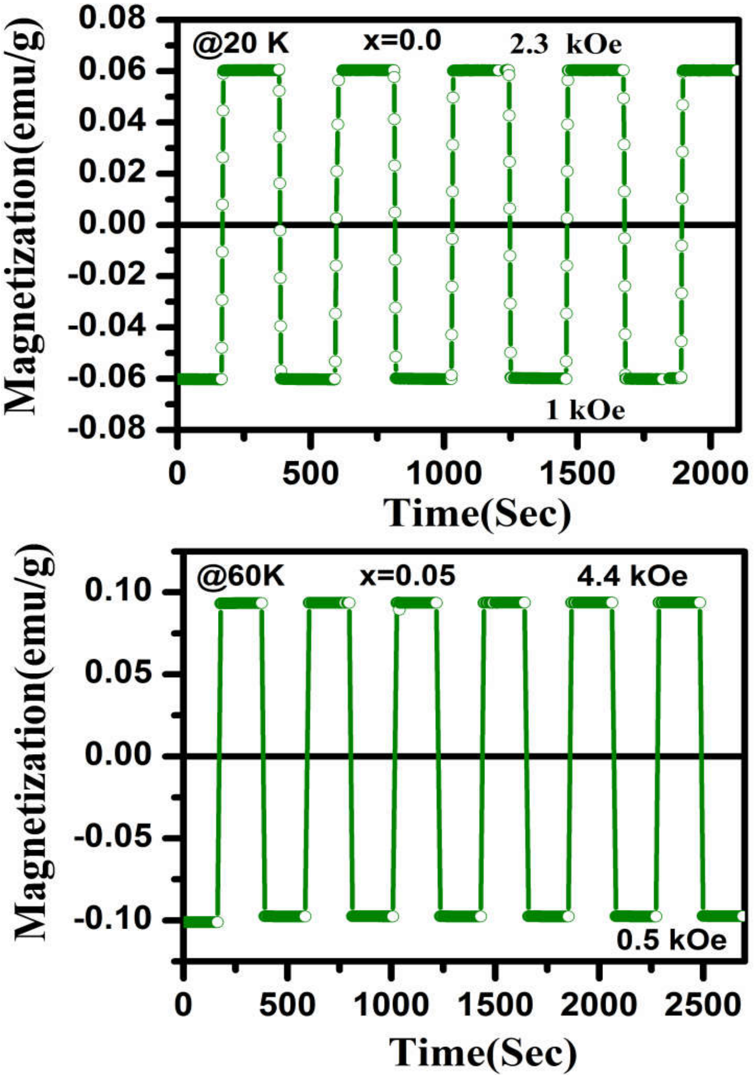

Figure 3.15 Bipolar magnetic switching behaviour in $CeCr_{1-x}Fe_xO_3$ (x = 0.0 and 0.05) with changing the magnitude of external magnetic field without change in direction.

The M_{FC} at 1 kOe show that the net magnetization is negative, whereas by switching the field to 2.3kOewhich is higher than the internal field of Cr^{3+}, Ce^{3+} moments are flipped in field direction and shows the positive magnetization. When the field is reversed back to 1 kOe, the internal field dominates over the external field due to which the Ce^{3+} moment flipped back to initial state causing the net magnetization to become negative. The magnetization is recorded for 200 sec at 20K for both fields, and switching behavior is repeated for five subsequent cycles. The bipolar switching effect for $x = 0.05$ is carried out at 60 K in between the field of 0.5 kOe and 4.4kOe. Here the switching behavior is observed due to flipping of Ce^{3+}+Fe^{3+} moment in dominated field direction. The repeatability of the switching behavior checked for several cycle, and it is found that the magnetization switching is reversible and steady. Without changing the direction of the magnetic field, switching of magnetic moments can be actuated between the negative and positive just by changing the magnitude of the magnetic field in the same direction. Such phenomenon demonstrates the potential application in magnetic switching, nonvolatile magnetic memory, and spintronics based devices.

3.6 Conclusion

We investigated the structural, optical, and magnetic properties of $CeCr_{1-x}Fe_xO_3$($x = 0$ and 0.05) compounds synthesized via nitrate solution combustion method. After increasing x to 0.05, bond length and lattice volume were increased. Transmission electron micrographs confirmed the particle size in nano range and an increase in particle size from ~45 nm to ~66 nm was demonstrated when x increased from 0 to 0.05. Tauc plot derived from optical absorption spectra revealed the decrease in the band gap from 2.9 to 2.6 eV due to increase in particle size. From magnetization vs. temperature, we revealed a decrease in Neel temperature from 260 to 253 K along with a new magnetic ordering at 315 K after doping. The magnetic ordering at 315 K while attributed to Cr^{3+}-O-Fe^{3+} AFM ordering, decrease in T_N could be ascribed to the decrease in super exchange bond angle Cr-O2-Cr. Further, T_{comp} and T_{SR} were increased by two-fold and we observed magnetization compensation below T_{SR} when x increases to 0.05. Such magnetic anomalies were understood based on the interaction between Cr^{3+}, Ce^{3+} and Fe^{3+} moments and their temperature dependent magnetic behavior. For the first time, we showed bipolar switching of magnetization in these compounds below T_{comp} by just varying the magnitude of magnetic field while keeping its direction fixed. Both the compound possesses the optical band gap in visible range and a stable magnetic switching behavior. Therefore, these materials can be used in photo-catalysis, spin resolving and magnetic switching devices.